JMEPEG (2022) 31:3445–3456
https://doi.org/10.1007/s11665-021-06441-5

TECHNICAL ARTICLE

Microstructural Variation and Corrosion Behavior of 60/40 Brass/Ti_2SC Surface Composite through Friction Stir Processing

Z.S. Mousavi, S. Karimi, A. Heidarpour, S.M. Hosseini, and S. Ghasemi

Submitted: 10 March 2021 / Revised: 24 September 2021 / Accepted: 8 November 2021 / Published online: 6 January 2022

In this paper, the Ti_2SC MAX phase was used as a reinforcement to produce 60/40 brass surface composites using friction stir processing (FSP). The effect of FSP and Ti_2SC MAX phase reinforcement particles on the electrochemical behavior of the brass alloy and its surface composite was studied in NaCl solution (3.5 wt.%). Microstructural features of the specimens were assessed by optical microscopy and scanning electron microscopy equipped with energy-dispersive spectroscopy. Also, the corrosion behavior of the base metal and FSPed samples with and without Ti_2SC particles was examined by different electrochemical methods such as cyclic polarization, potentiodynamic polarization, and electrochemical impedance spectroscopy. The FSP caused grain refinement and homogeneous distribution of Ti_2SC particles in the brass matrix. The results revealed that the presence of reinforcement particles and the number of FSP passes had considerable effects on the corrosion resistance of the specimens. For FSPed samples with or without reinforcement particles, corrosion resistance decreased by increasing the pass number from 1 to 3. The corrosion current density of brass alloy was 12.5 $\mu A.cm^{-2}$, while this value exceeded 30 $\mu A.cm^{-2}$ for all FSPed samples after FSP.

Keywords corrosion behavior, Cu-40 wt.%Zn, cyclic polarization, electrochemical impedance spectroscopy, friction stir processing

1. Introduction

Brass has been widely employed in electrical applications, power transmission, chemical, marine industry, water distribution networks, and tubing due to its high electrical and thermal conductivity (Ref 1, 2). However, copper alloys are highly susceptible to corrosion in corrosive environments containing chloride (Ref 3), nitrate (Ref 4), and ammonia (Ref 5). There are increasing reports of pitting and dezincification corrosion as the main factor in brass demolition. Most of the data on the corrosion of the pitting corrosion of brass are reported in the chloride-containing solutions (Ref 6, 7). The corrosion has severely limited the life and application of brass. Therefore, it is not surprising that the improved corrosion resistance of metal has been the center of focus in many studies (Ref 8-11). Many of these investigations dealt with inhibition of copper and its alloy corrosion in chloride solutions (Ref 10, 12-15). In the industry, some approaches, such as magnetron scattered ion coatings (Ref 16), polymer coatings (Ref 17), and electrochemical coatings (Ref 18), have been employed to reduce the corrosion rate of brass.

However, some of these methods fail in maintaining their performance in seawater or harm the environment. Therefore, the main challenge to protect copper alloys is to use an environmentally friendly and low-cost anti-corrosion method. Friction stir processing (FSP) is a process in which a solid-state technique is used to modify the surface and microstructure of materials. This technique is developed on the primary principles of friction stir welding (FSW) (Ref 19). The benefits of the FSP method include grain refinement, the ability to fabricate surface composite, and also modifying the microstructure of materials, e.g., removing the casting and forging defects. Moreover, improvement in the mechanical properties such as tensile strength, hardness, fatigue, as well as abrasion resistance and corrosion behavior can be achieved by this process (Ref 20). In this method, internal channels or surface grooves are used to add reinforcing particles to the substrate (Ref 19). During FSP, the temperature increases due to the severe plastic deformation induced by rotation and friction between the tool and the workpiece (Ref 21). The friction heating and severe plastic deformation imposed by FSP leads to considerable microstructure changes, which comprises three distinct regions, namely: the heat-affected zone (HAZ), the thermomechanically affected zone (TMAZ), and the stir zone (SZ) (Ref 22).

In recent years, MAX phases (with the general formula of $M_{n+1}AX_n$) have emerged as a new group of ceramic materials with a layered structure has been identified in which M stands for an early transition metal, A denotes an element of group A (often IIIA and IVA), and X represents carbon or nitrogen. This category of materials has a unique structure and properties (Ref 23). While they behave as metal in terms of machining, electrical and thermal conductivity, similar to ceramics, they are resistant to oxidation and corrosion. Ti_2SC MAX phase has the

---

Z.S. Mousavi, S. Karimi, A. Heidarpour, S.M. Hosseini, and **S. Ghasemi**, Department of Metallurgy and Materials Engineering, Hamedan University of Technology, 65155-579 Hamedan, Iran. Contact e-mail: heidarpour@hut.ac.ir.

lowest c-lattice parameter among other MAX phase compounds. Owing to its layered structure, Ti_2SC has revealed better lubrication properties similar to graphite and MoS_2 (Ref 24, 25).

The use of Ti_2SC MAX phase as a reinforcement of metal base composite is a fascinating idea as this phase could improve some properties such as tribological behavior. Before dealing with tribology, the corrosion behavior of brass-Ti_2SC should be evaluated. In this context, the main objective of this study is to assess the effect of FSP pass numbers and the addition of Ti_2SC MAX phase on the corrosion behavior of 60-40 brass alloy. According to our studies, such items have not yet been studied and should be investigated. The microstructural changes after FSP with/without Ti_2SC reinforcement, as well as its electrochemical behavior, were investigated.

2. Experimental

In this study, to prepare specimens, the appropriate size of 60/40 brass sheets with dimensions of $100\times50\times4$ mm^3 was cut. The surface of the plates was polished and cleaned before FSP. The FSP machine employed in the experiments was a horizontal-reinforced milling machine. A cylindrical pin made of WC, with a 4 mm length, 5 mm diameter, and 17.5 mm shoulder diameter was used in the experiments. The rotation speed, movement velocity, immersion depth, and tilt angle were 1000 rpm, 56 mm/min, 3 mm, and 2°, respectively. The FSP was performed at room temperature. These parameters were selected for FSP from several combinations of rotational and transverse speeds to obtain flawless specimens with the best properties.

Two specimens with Ti_2SC reinforcement were subjected to FSP for 1 and 3 passes, which were named as 1-pass FSPed surface composite and 3-pass FSPed surface composite. The Ti_2SC MAX phase was synthesized as reported in the previous work (Ref 26). The Ti_2SC particles were packed in a groove in the middle of the specimen before FSP. For comparison, two samples were treated without reinforcement for 1 and 3 passes, named as 1-pass FSPed BM and 3-pass FSPed BM.

The microstructure of the FSPed samples was observed with an optical microscope of the Union equipped with a digital optical scanner. The composition of the etchant includes iron chloride. The microstructural characterization of the friction stirred samples was analyzed by a scanning electron microscope (Jeol, JSM 840). The SEM was equipped with energy-dispersive spectroscopy (EDS). The phase analysis of the samples was carried out by X-ray diffraction (XRD, Asenware AW-DX300, Cu target, Kα radiation, 40 KV and 30 mA), at a scanning step of 0.05° and time per step of 1 s.

Electrochemical measurements were carried out using a conventional three-electrode-electrochemical cell in a Potentiostat set (Iviumstat compact 20250 H) controlled by Ivium soft electrochemistry software. Measurements were performed at the ambient temperature and atmosphere. The sample was used as working electrodes; Pt and Ag/AgCl electrodes served as the counter and the reference electrodes, respectively. All the potentials reported in this research were measured vs. the Ag/AgCl reference electrode.

The test solution was 3.5% NaCl solution at room temperature at a pH value of 7.5-8. Before each electrochemical experiment, the surface of the samples was polished. Then, the electrode was washed with distilled water several times to remove the physisorbed particles, followed by drying. To ensure reproducibility, all the experiments were started after reaching the open circuit potential (OCP). All electrochemical tests (including Tafel, CV, and EIS analysis) were only started after the OCP reaching within ±5 mV. To draw cathodic and anodic polarization (Tafel) curves of the brass specimen, current values were recorded in the range−2.0 to +2.0 V vs. Ag/AgCl at a constant scanning rate of 1 mV/s, which was then converted to current density by figuring the surface area. Cyclic polarization tests were carried out for the brass electrode negative to positive in the potential range of −2.0 to +2.0 V versus Ag/AgCl at a constant scan rate of 1 mV/s. In addition, electrochemical impedance spectra (EIS) experiments were performed in the frequency range of 10^5 to 10^{-1} Hz at OCP.

3. Results and Discussion

3.1 Microstructural Evaluation

Figure 1 depicts the SEM micrographs of the 60-40 brass alloy, cross section of the FSPed samples, and the 1-pass FSPed surface composite. As seen in Fig. 1(a), the 60-40 brass alloy consists of α and β brass with small amounts of porosity. It should be noted that the heat-affected zone (HAZ) was not seen in the microstructures, which may be due to low heat input of FSP and high thermal conductivity of base alloy. By applying FSP to the surface of brass alloy, the heating of friction and severe plastic deformation led to major evolution in the microstructure. At first, in all cases, there was a very well-bonded between stirring zone and base alloy, with no defects, including voids or cracks. After FSP, the dual phase of the brass was retained, but the refinement of the grain structure occurred in the stir zone of 60/40 brass (Fig. 1b). Figure 1(c) depicts the SEM micrograph of the 1-pass composite surface. This SEM micrograph was taken in backscatter mode and clearly shows three distinct areas: the gray matrix, the black phase, and a small white areas. These small white areas are Ti_2SC MAX phase particles dispersed in the 60-40 brass alloy as confirmed by an EDS spectrum in Fig. 1(d). The good dispersion of the Ti_2SC second phase could be seen with no agglomeration. The particles did not agglomerate around the grain boundary regions to form a typical network segregation. Actually, in contrast to casting methods, the frictional heat did not have enough energy to completely melt the brass matrix, and thus segregation did not occur.

During the FSP, a severe increase in temperature and plastic deformation led to the arrangement of fine equiaxed grains in the SZ (Ref 27). An increase in temperature can result in annealing and grain growth within the SZ or lead to the formation of dynamic crystallized grains and a reduction in grain size in the SZ. In addition to dynamic recrystallization, the presence of reinforcement also refined the grain. Reinforcing particles prevented the growth of newly crystallized grains by several mechanisms, such as the pinning effect or particle dragging (Ref 28). Therefore, in this case, grain refining due to dynamic recrystallization and grain growth due to significant heat input are two competitive processes (Ref 29).

Figure 2 depicts the optical micrographs of the stir zone cross-section of 1 and 3 passes FSPed samples with or without

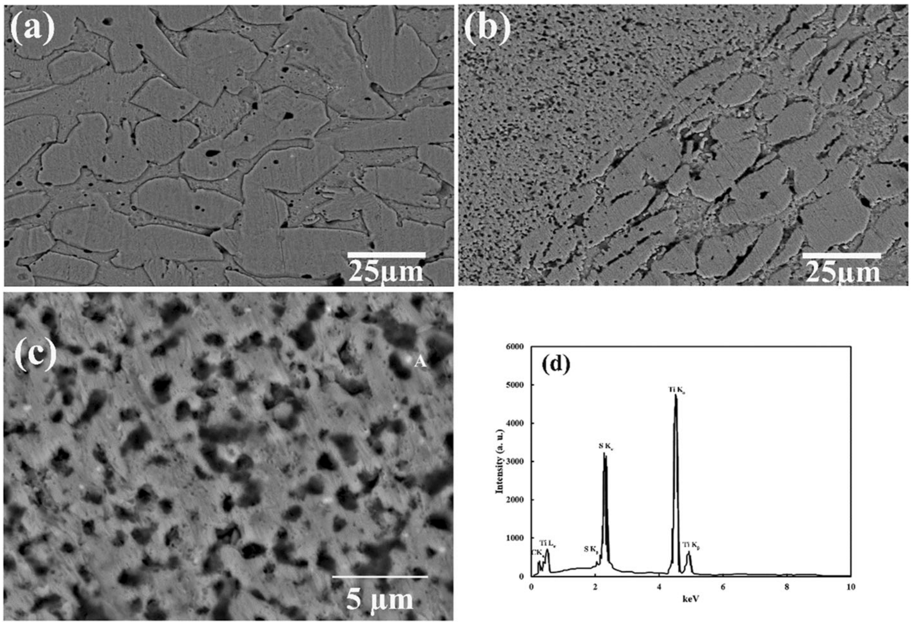

Fig.1. SEM image of (a) 60/40 brass, (b) the stir zone and base metal boundary, (c) 1-pass FSPed surface composite, (d) EDS spectrum of white point A in Fig. 1c indicating Ti_2SC MAX phase particle

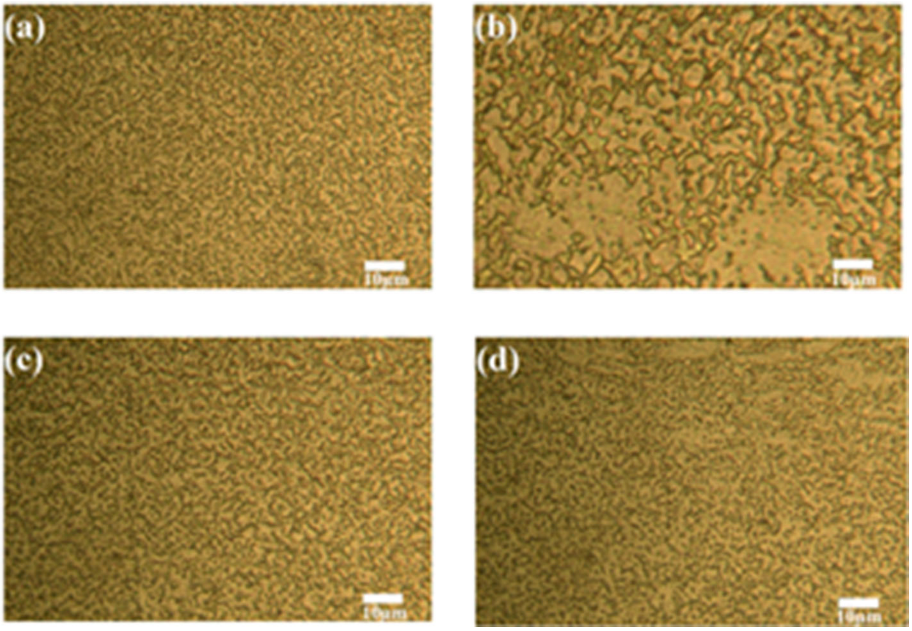

Fig. 2. OM micrographs of stir zone (a) 1-pass FSPed BM, (b) 3-pass FSPed BM, (c) 1-pass FSPed surface composite, and (d) 3-pass FSPed surface composite

reinforcement. A considerable grain refinement could be observed for all samples after FSP. In this case, modification and refinement of the grain structure occurred in the SZ, which decremented the grain size in that area. It seems that for the 3-pass FSPed samples, in addition to recrystallization, annealing and grain growth also occurred due to increasing temperature and plastic deformation after 3 passes. However, the 3-pass FSPed surface composite showed no grain growth due to the presence of Ti_2SC reinforcement. In this case, Ti_2SC particles inhibit the grain boundary mobility, and hence they considerably limited the grain growth.

3.2 Corrosion Behavior

3.2.1 Open Circuit Potential. To ensure the reproducibility of the corrosion tests, the working electrode was allowed to reach the OCP. The OCP magnitude for samples is a precise sign of their electrochemical activity (Ref 30). Figure 3 shows the OCP evolution of the base metal and all of the FSPed samples with and without Ti_2SC powder in the NaCl solution. As indicated in Fig. 3, the 1-Pass FSPed BM, 1, and 3-pass FSPed composite specimens required less time to reach the stable OCP values, while the BM and 3-Pass FSPed BM

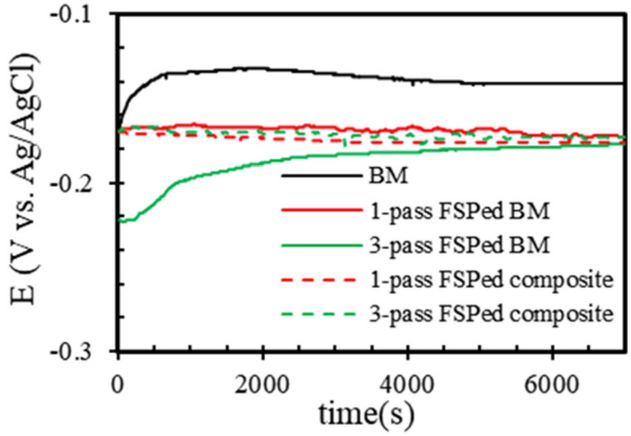

Fig. 3. Open circuit potential vs. time for all samples measured in 3.5 wt% NaCl solution at 25 °C

sample seem to need more time to reach a stable OCP value. This figure also indicates that the steady-state potential of FSPed samples shifts to more negative values compared to the base alloy, which is a sign of increased corrosion susceptibility of FSPed samples.

Moreover, in FSPed BM samples, the steady-state potential shifted to more negative values by increasing FSP pass numbers. This indicates that increasing the number of passes enhanced the corrosion susceptibility. The 1-pass and 3-pass FSPed composite samples had a similar trend, as with an increasing FSP number, the steady-state potential remained almost constant with no significant variation.

3.2.2 Polarization Diagrams. Figure 4 shows the polarization diagrams for all specimens. Moreover, Table 1 summarizes the electrochemical parameters obtained from Fig. 4. The corrosion potential values of 1-pass FSPed BM and 3-pass FSPed BM are lower than the base alloy, while these values are higher for surface composites compared to the base alloy value. Corrosion potential is defined as the force required by a corrosion reaction (Ref 28). The more negative the potential, the greater the corrosion tendency of the material (Ref 9). Also, all FSPed samples showed high corrosion current densities, indicating a continuous enhancement in the corrosion rate of the specimens, and the minimum corrosion rate of the base alloy. It could be said that the corrosion resistance of brass was degraded by the application of FSP. The increase in corrosion susceptibility and corrosion rate can be attributed to residual stresses after FSP and the high density of the grain boundary. Moreover, Op't Hoog et al. reported that the residual stresses generated after grain refinement depend on electrochemical behavior (Ref 31). During FSP, the surface layers of the alloy are exposed to severe plastic deformation, mixing, and significant frictional heating, leading to a very fine and equiaxed grain microstructure due to dynamic recrystallization in the stirred zone (Ref 22). In the other words, during FSP, the grain refining of the surface layer is refined (Ref 32). The fine-grained structure has a high density at the grain boundary, and because the grain boundaries are more active in terms of corrosion activity than grains, the corrosion potential FSPed sample becomes more negative compared to the base metal (Ref 33).

The effect of the addition of the second phase on the corrosion resistance of metal matrix composites is a controversial issue. The addition of ceramic particles improves the corrosion resistance in some cases, while it deteriorates the resistance in others. Here, two distinct phenomena are involved: friction stir processing and incorporating Ti_2SC MAX phase. The application of FSP on the surface of 60-40 brass alloy resulted in grain refinement which led to the considerable grain boundary. The grain boundaries are active sites and promote corrosion. The corrosion rate of the brass alloy increases from 12.5 to above 30 $\mu A.cm^{-2}$ for FSPed specimens. This shows the effect of FSP on the corrosion of brass alloy. On the other hand, the corrosion rate of the FSP composite surface is higher than that of the brass alloy, but is similar to that on the FSPed surface without adding Ti_2SC MAX phase. Also, the presence of reinforcing particles in composite samples led to some discontinuities in the surface oxide layer and local and galvanic corrosion on the composite surface, which can explain the decrease of corrosion resistance of surface composites (Ref 34). The presence of reinforcing particles led to an increase in the surface heterogeneity (Ref 35).

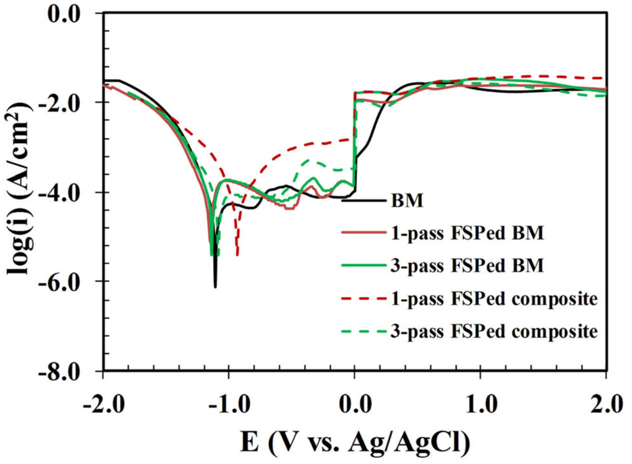

Fig. 4. Potentiodynamic polarization curves of base alloy and FSPed samples

3.2.3 Cyclic Potentiodynamic Polarization. Figure 5 shows the cyclic polarization curves in the NaCl solution for all samples. The polarization curve of these samples showed 3 anodic peaks and 3 cathodic peaks. Brass and copper alloys had similar anodic behaviors and showed a limiting diffusion process during anodic scanning, while the behavior of zinc was different (Ref 36). The corrosion potential of copper, Cu-40Zn alloy, and zinc were −0.235, −0.210, and −1.08, respectively (Ref 37). Zinc in the brass dissolved in a corrosive solution due to its electronegativity relative to the copper (Ref 6). The oxidation of copper occurred at higher potentials (Ref 38). The initial stage of the anodic oxidation of brass involved the preferential dissolution of the less noble component, i.e., zinc, almost without the copper dissolution. (Ref 39). The kinetics and mechanism of anodic dissolution and film formation of brass during brass corrosion in NaCl can be occurred according to the following reactions.

In the first stage of brass corrosion, dezincification of brass occurs at the corrosion potential, giving rise to ZnO formation according to the following reaction (Ref 7).

$$Zn + H_2O = ZnO + 2H^+ + 2e^- \qquad \text{(Eq 1)}$$

Table 1. The corrosion parameters of the base alloy (BM) and FSPed samples

Sample	E_{corr}, V vs. Ag/AgCl	i_{corr}, μA.cm^{-2}
BM	−1.10	12.5
1-pass FSPed BM	−1.16	20.0
3-pass FSPed BM	−1.14	31.2
1-pass FSPed surface composite	−0.92	31.6
3-pass FSPed surface composite	−1.08	33.0

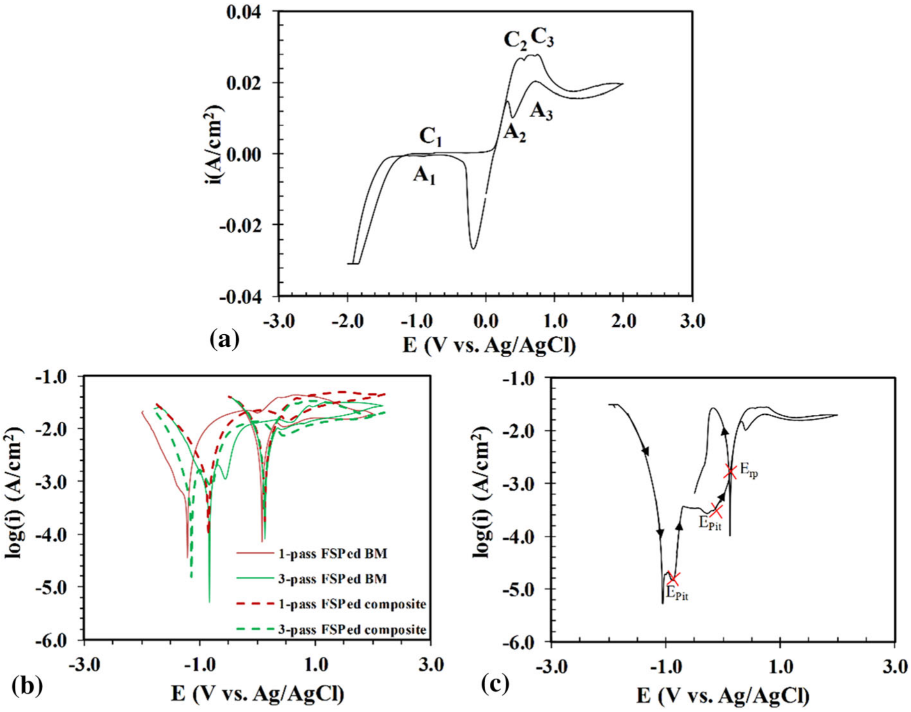

Fig. 5. Cyclic polarization curves of (a) base metal, (b) FSPed samples, and (c) the indication values of corrosion potential (E_{corr}), pitting potentials (E_{pit}), and repassivation potentials (E_{rp})

The voltammogram of the samples shows a broad region (A_1) at highly negative potentials, which is related to zinc corrosion of brass, namely dezincification, and formation of ZnO (Ref 38). In the next step, a bilayer film is formed, encompassing an inner layer (Cu_2O), and CuO or $Cu(OH)_2$ as the outer layer (Ref 38). The small anodic peak (A_2) corresponds to the formation of the Cu_2O film, and Cu_2O is directly obtained from the copper via a two-electron transfer reaction through the oxidation of Cu to Cu_2O (Ref 7, 40, 41) according to the following reaction:

$$2Cu + H_2O = Cu_2O + 2H^+ + 2e^- \qquad \text{(Eq 2)}$$

The A_3 peak is related to the formation of the $Cu(OH)_2$ or CuO layer (Ref 42-44). Thus, peak A_3 is associated with the following reactions:

$$Cu + 2OH^- = Cu(OH)_2 + 2e^- \qquad \text{(Eq 3)}$$

$$Cu(OH)_2 = CuO + H_2O \qquad \text{(Eq 4)}$$

$$Cu_2O + H_2O = 2CuO + 2H^+ + 2e^- \qquad \text{(Eq 5)}$$

The above-mentioned reactions led to the formation of an oxide bilayer consisting of Cu_2O as the inner layer, and hydrated CuO as the outer layer. The final structure is specified as $Cu/Cu_2O/CuO$ (Ref 40).

Similarly, the cathodic peaks are interpreted as:

(a) A shoulder peak of C_3, corresponding to the reduction of the outer CuO oxide to Cu_2O (Ref 45)
(b) A shoulder peak of C_2, including the reduction of Cu_2O to Cu (Ref 45)
(c) The broad region of C_1 attributable to the ZnO reduction to Zn (Ref 45)

The above reactions with standard potentials may occur on the metal surface (Table 2).

Breakdown potential is a measure of the onset of pitting; thus materials with more positive breakdown potentials have better pitting resistance (Ref 48). Several methods have been used to determine this value.

The most positive potential in the anodic polarization curves was 0.2 mV/s where the anode current was still in the limiting diffusion process (Ref 45). The specific potential at which the current begins to increase is called the breakdown potential (Ref 49). Another method used to determine the E_b is the extrapolation toward zero potential scan rate (Ref 50). In this study, similar to Mikic et al. (Ref 40), interception of tangential

Table 2 Standard equilibrium potentials of redox processes related to copper and zinc in base solutions containing chloride ions (Ref 46, 47)

Reaction	E^0, V
$Zn+H_2O = ZnO+2H^{+}+ 2e^{-}$	−1.1
$2Cu+ H_2O = Cu_2O+2H^{+}+ 2e^{-}$	0.46
$Cu_2O+H_2O = 2CuO+2H^{+}+ 2e^{-}$	0.67
$Cu_2O+3H_2O = 2Cu(OH)_2+2H$	0.73

Table 3. The corrosion parameters of the samples (V vs. Ag/AgCl) obtained from cyclic polarization

Sample	$E_{pit}(1)$	$E_{pit}(2)$	E_{rp}	$E_{pit}-E_{rp}$
BM	−0.85	0	0.10	0.95
1-pass FSPed BM	…	0.35	−0.10	0.45
3-pass FSPed BM	−0.85	0.35	−0.10	0.75
1-pass FSPed composite	…	0.35	−0.10	0.45
3-pass FSPed composite	−0.75	0.35	0.05	0.70

at the point of a sudden increase in current density of the cyclic polarization was considered as the breakdown potential.

The values of corrosion potential (E_{corr}), pitting potentials (E_{pit}), and repassivation potentials (E_{rp}) are listed in Table 3. These values were determined based on Fig. 5c. The breakdown potential (E_{pit}) values of all FSPed samples were higher than that of the base metal, implying higher pitting resistance of FSPed samples compared to the base metal.

Repassivation potential is defined as a potential at which the growth rate of pits is stopped. The amount of hysteresis or the difference between E_{pit}-E_{rp} indicates the localized corrosion. In general, the larger hysteresis loop (E_{pit}-E_{rp}) indicates the probability of pitting corrosion and leads to a greater amount of localized corrosion (Ref 51). According to Table 3, the ($E_{pit}-E_{rp}$) value of all FSPed samples was less than the base metal. Therefore, the amount of localized corrosion and the susceptibility of the material to the pit corrosion of all FSPed samples are less than those of the base metal.

Comparing base metal FSPed samples, using FSP on brass shifted the pitting potential toward less positive (noble) values. The (E_{pit} -E_{rp}) value is also higher for the base metal. The electrochemical evaluation of localized corrosion showed that the pitting potential was more positive in the FSPed samples. Also, the repassivation was easier.

Furthermore, the (E_{pit}-E_{rp}) value of 3-pass FSPed samples (with or without reinforcement-Ti_2SC) was more than 1-pass FSPed samples. Increasing the number of FSP passes enhanced the pitting corrosion tendency of FSPed samples. Therefore, it can be said that the amount of localized corrosion of 3-pass FSPed samples is more than 1-pass FSPed ones. These results can be attributed to the separation of impurities from the grain boundary or the creation of concentration gradients of alloying elements due to annealing. As mentioned before, increasing the number of FSP passes caused annealing and separation of impurities to the grain boundary. Therefore, a gradual increase can be detected in localized corrosion by enhancing the number of FSP passes. Thus, the higher amount of localized corrosion of the specimens with an increasing pass number can be related to the annealing and separation of impurities to the grain boundary.

Additionally, the presence of reinforcing particles did not affect pitting corrosion behavior. According to Table 3, the E_{pit} and (E_{pit}-E_{rp}) value of 1-pass without Ti_2SC MAX phase particles specimen were equal to 1-pass reinforced composite sample and also, the E_{pit} and (E_{pit}-E_{rp}) of 3-pass without Ti_2SC MAX phase particles specimen were equal to 3-pass reinforced composite sample.

3.2.4 Electrochemical Impedance Measurement. To further assess the electrochemical behavior of the FSPed brass, the electrochemical impedance spectroscopy (EIS) test was performed in NaCl solution (3.5 wt.%). The Nyquist plots of the base alloy and FSPed brass are depicted in Fig. 6. Generally, the Nyquist impedance spectra in Fig. 6(a) show one time-constant with the complicated electrochemical process. Typically, the presence of the imperfect loop is usually related to the formation of an oxide layer on the brass alloy in NaCl solution. As observable in Nyquist plots (Fig. 6), all of the samples showed a capacitive loop. The diameter of this capacitive loop is equal to the polarization resistance of the working electrode during corrosion (Ref 9). Therefore, increasing the diameter of the capacitive loop presents an increase in corrosion resistance (Ref 9).

Figure 7 depicts the equivalent circuit model used to fit the impedance spectra. The electrical parameters of this equivalent circuit are given in Table 4. The Chi-square (χ^2) value shows the fitting accuracy to the equivalent circuit; the lower the χ^2 values, the better fitting to the experimental data. The circuit included a solution resistance (R_s), R_{ct} represents the charge transfer resistance and CPE of the double layer (Q_{dl}). CPE shows the deviations from an ideal capacitance behavior, which involved two parameters: an admittance (Y_0) and empirical constant (n, ranging from 0 to 1), both of which are usually assumed to be frequency independent (Ref 52, 53). In this circuit, a constant phase element was used to consider the uneven surface resulting from the roughness of the metal surface (Ref 13).

The corrosion resistance values of all FSPed specimens are lower than those of the base alloy. Therefore, the corrosion resistance of brass was degraded after FSP. The increase in corrosion susceptibility and corrosion rate can be attributed to residual stresses after FSP and the high density of the grain boundary. Also, as seen from Fig. 6, by increasing FSPed pass numbers, the diameter of the semi-circle decreases. Therefore, it may be said that the corrosion resistance of samples significantly decreased by increasing FSPed pass numbers. Moreover, the presence of reinforcing particles reduced corrosion resistance, indicating an increase in localized corrosion was observed by adding reinforcement particles.

By increasing FSP passes, the R_{ct} values declined, whereas Y_0 values tended to increase. The values of R_s varied in the range of 4.83-8.19 $\Omega.cm^2$, which is approximately low for all samples. R_{ct} indicates the corrosion rate of the sample; the higher the R_{ct} value, the lower is the corrosion rate (Ref 46). In other words, increasing the R_{ct} value indicates a decrement in the dissolution rate of the metal after immersion in the neutral salt solution (Ref 54). Furthermore, the increase in R_{ct} indicates a higher resistance to active dissolution (Ref 55). As shown in Table 4, the R_{ct} value of Cu-40wt%Zn base metal is 19000 $\Omega.cm^2$. Specifically, for the FSPed sample without powders, the R_{ct} value of the 1-pass decreased to 14712 $\Omega.cm^2$, and as the FSP pass was increased to 3-pass, it further declined and reached 3356 $\Omega.cm^2$. The decrement in the charge transfer resistance value for 1-pass and 3-pass FSPed samples fairly

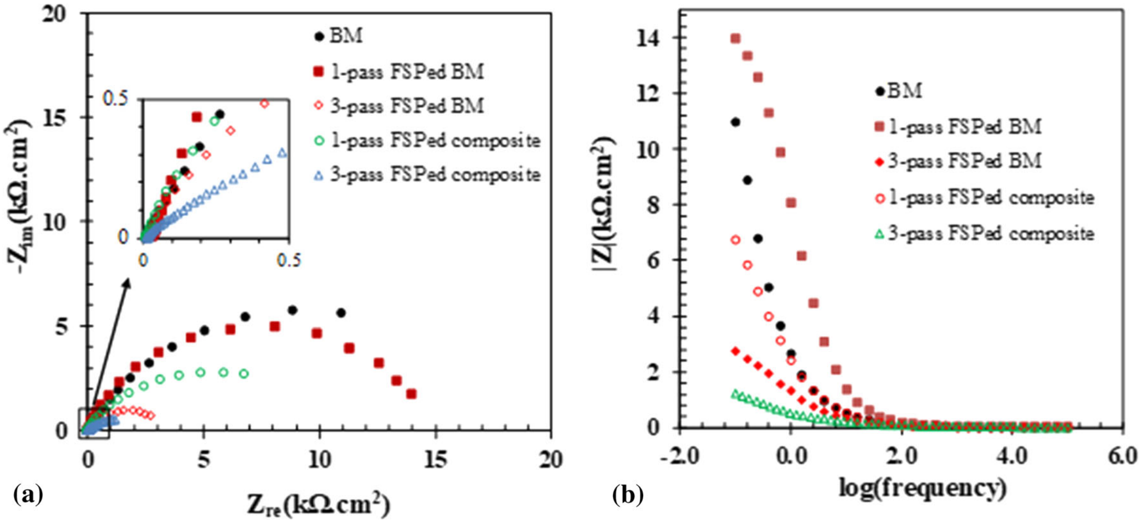

Fig. 6. EIS results of BM and FSPed samples in 3.5% NaCl solution: (a) Nyquist plots; (b) Bode plot

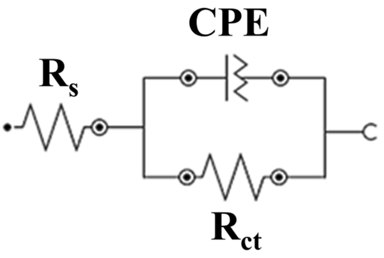

Fig. 7. The equivalent electrical circuit for BM and FSPed samples

correlates with polarization results. As shown in Table 1, the i_{corr} of FSPed samples drastically increased from 12.5 for BM to 20.0 and 31.22 µA.cm^{-2} in 1-pass and 3-pass FSP, respectively.

The presence of reinforcing particles affected the electrochemical behavior. The electrochemical resistance (R_{ct} value) of FSPed composite samples was lower than FSPed BM samples. The 1-pass reinforced composite specimen revealed poor corrosion performance compared with the 1-pass without Ti_2SC MAX phase particles. The R_{ct} value of the 1-pass FSPed BM sample was 14700 Ω.cm^2 which decremented to 10000 Ω.cm^2 for the 1-pass FSPed sample with powders. Moreover, the R_{ct} value of the 3-pass FSPed BM sample was 3356 Ω.cm^2, which reduced to 2735 Ω.cm^2 in the 3-pass FSPed sample with powders. The decrement in the corrosion resistance of 1-pass and 3-pass FSPed composite samples was confirmed by polarization results. It can be concluded that the addition of Ti_2SC MAX phase particles and performing a FSP decreased the corrosion resistance of Cu-40wt% Zn.

Another way to present EIS test results is to use bode diagrams. In bode plots, the impedance value at the lowest frequency represents the total resistance of a system (Ref 28). At low frequencies, the higher the impedance, the better the corrosion resistance (Ref 56). From Fig. 6(b), the impedance values at the lowest frequency are lower for the FSPed composite and FSPed BM samples as compared with BM, implying a decrease in corrosion resistance of the FSPed samples. Based on Fig. 6(b), the impedance values of the 1-pass FSPed samples are higher than the 3-pass FSPed samples, suggesting a decline in corrosion resistance with enhancing the number of passes.

The thickness of the film or double layer which formed on the working electrode surface can be measured by EIS data. The method involves the measurement of the effective capacitance of the electrical double layer using the following equation:

$$d = \frac{\varepsilon_0 \varepsilon A}{C_{eff}} \quad \text{(Eq 6)}$$

where ε is the dielectric constant of the film or double layer on the brass electrode and ε_0 represents the vacuum dielectric permittivity (8.85×10^{-14} F cm^{-1}), A is the effective surface area, and d denotes the film or double-layer thickness. For the film or double layer, the chosen value of the dielectric constant was 7.9, which is an average of zincite (8.15) and cuprite (7.6) (Ref 57). According to Mohammadi's work (Ref 58), the calculation of film or double-layer thickness of the working electrode are likely to be very important in corrosion studies. In the present study, three approaches were used to calculate the thickness of the film or double layer: (a) normal distribution model (H-M) (Ref 40), (b) Brug's Model (Ref 41), and (c) power law (PL) model (Ref 42).

H-M model—Hsu and Mansfeld developed the capacitance calculation using the following equation:

$$C_{\mathrm{eff}} = Y_0^{\frac{1}{n}} \cdot R_{ct}^{\frac{1-n}{n}} \quad \text{(Eq 7)}$$

where R_{ct} shows the resistance of charge transfer layer and n is the exponent of CPE. In this model, a normalized probability distribution of time constants is used in systems including conductive dispersion and a dielectric like organic coating, oxide films and rough-porous surfaces (Ref 40, 42).

Brug's model—The surface distribution of time constants has been assumed in this model. According to Brug's model, surface inhomogeneity is included the distribution of the double-layer capacitance of the entire surface. The capacitance of film or double layer related to CPE parameters can be determined by the following equation:

Table 4. The values of the equivalent circuit parameters of Fig. 6

Sample	R_s, Ω.cm^2	R_{ct}, Ω.cm^2	Y_0, μF.cm^{-2}	n	χ^2
BM	7.61	19000	57.59	0.70	0.002
1-pass FSPed BM	8.57	14712	14.80	0.77	0.003
3-pass FSPed BM	5.88	3356	126.00	0.67	0.001
1-pass FSPed composite	5.70	10000	87.27	0.65	0.002
3-pass FSPed composite	10.28	2735	542.00	0.47	0.004

Table 5. Calculated values of capacitance of double layer via different models

Sample	H-M model C_{dl}, μF cm^{-2}	Brug's model C_{dl}, μF cm^{-2}	P-L model C_{dl}, μF cm^{-2}
BM	59.856	2.094	0.098
1-pass FSPed BM	9.386	1.014	0.108
3-pass FSPed BM	82.462	3.616	0.115
1-pass FSPed composite	81.100	1.452	0.053
3-pass FSPed composite	844.851	1.550	0.009

Table 6. Calculated thickness of films formed on Brass electrode surface using different methods

Sample	H-M model d, nm	Brug's model d, nm	P-L model d, nm
BM	0.1168	3.3385	71.5855
1-pass FSPed BM	0.7448	6.8921	64.9748
3-pass FSPed BM	0.0848	1.9335	60.6936
1-pass FSPed composite	0.0862	4.8141	132.0535
3-pass FSPed composite	0.0083	4.5098	809.6309

$$C_{\mathrm{eff}} = Y_0^{\frac{1}{n}} \cdot \left(\frac{1}{R_s} + \frac{1}{R_{ct}}\right)^{\frac{n-1}{n}} \qquad \text{(Eq 8)}$$

Power law (P-L) model—The capacitance of the double layer can be measured by normal distribution even if resistivity alters through the film thickness. This model is a powerful approach for the interpretation of physical features like dielectric constant, resistivity, and film or double-layer thickness as the following equation:

$$C_{\mathrm{eff}} = gY_0.(\rho_0 \varepsilon \varepsilon_0)^{1-n} \qquad \text{(Eq 9)}$$

where ρ_0 is the boundary value of resistivity at the interface (500 Ω.cm) and g denotes a numerically evaluated function of the CPE exponent as follows:

$$g = 1 + 2.88(1-n)^{2.375} \qquad \text{(Eq 10)}$$

Table 5 shows the calculated capacitances of the double layer on the brass alloy according to each of the three above-mentioned approaches. From Table 5, capacitances range was enhanced in the order of Power law (P-L) model> Brug's model> H-M model. The values of film layer thickness measured using C_{dl} values (via Equation 6) are demonstrated in Table 6 based on each proposed model from which C_{dl} was calculated. On the basis of literature studies, the thickness of film layer formed on a brass (60/40) surface was found to be typically 3-5 nm (Ref 40, 59, 60). According to the obtained result of Brug's model, the Brug's model is the only approaches that predicts the thickness of the film layer on the brass alloys within above-mentioned range.

3.2.5 Surface Characterization After Corrosion Test. The morphology and the main components of the brass surface after the corrosion test were analyzed by SEM and EDS techniques. Figure 8 depicts SEM micrographs of all samples after the polarization corrosion test. In addition, the EDS spectra of the samples are included in this figure. It can be seen that the brass surface was covered by poor corrosion products. The EDS results showed that the corrosion products were mainly composed of C, O, Cu, and Zn, indicating that the corrosion products on the surface of brass were mainly zinc and copper compounds. The presence of Ti should be due to the existence of Ti_2SC MAX phase particles on the composite surfaces. All specimens were seriously corroded, and pitting could be easily seen. The brass alloy after the corrosion test showed large grains with a typical feature of dezincification. The surface appeared as a porous layer, which was most probably formed by the selective dissolution of zinc. The FSPed specimens had more pits on their corroded surface, while the 1-pass FSPed composite exhibited uniformity. The pits in a broad range of size could be detected on the surface of FSPed samples. As discussed above and seen in Fig. 8, the resistance of the pitting corrosion of FSPed samples is less than that of the base metal.

The XRD patterns of the corroded 1 and 3-pass FSP composite surface are presented in Fig. 9. The XRD pattern of the brass alloy is also included for comparison. The XRD pattern shows the main phases of 60-40 brass, both α and β′ phases. After FSP, no phase transformation was detected in the 60-40 brass alloy. No peaks of the Ti_2SC MAX phase were detected due to its too low content. Some minor peaks could be

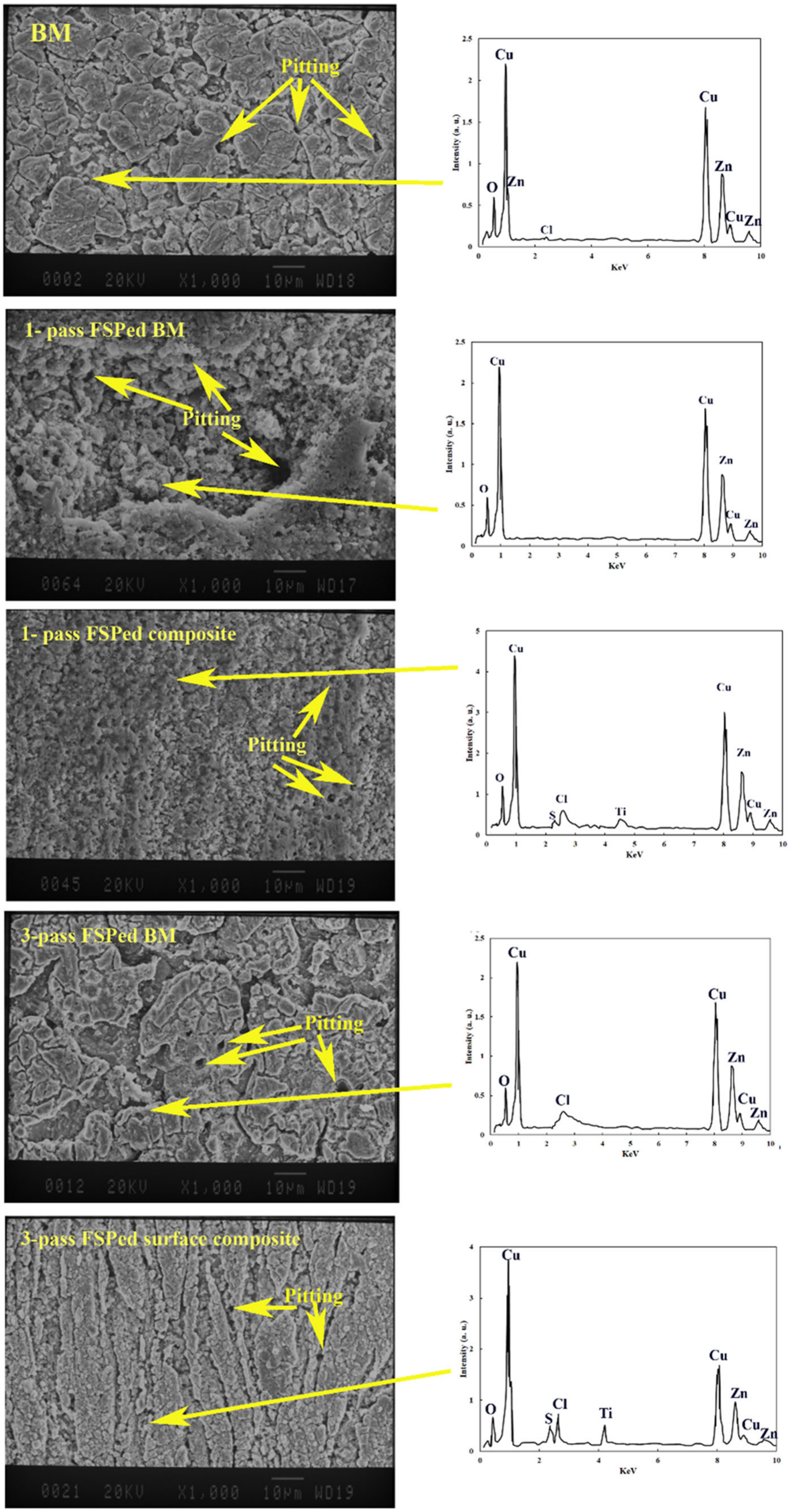

Fig. 8. SEM micrographs and EDS spectra of corroded specimens after corrosion test.

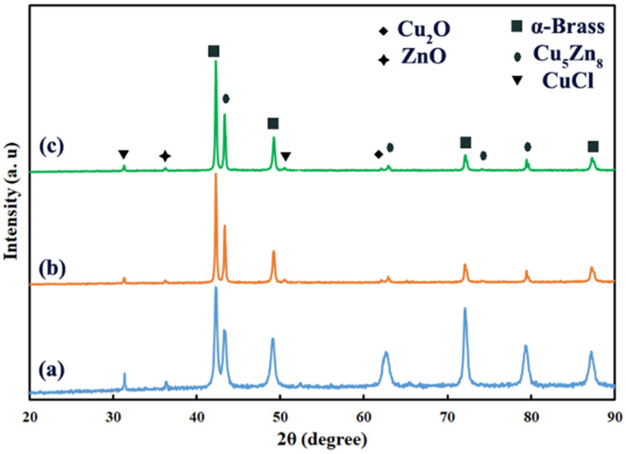

Fig. 9. XRD patterns of (a) 60-40 Brass, (b) 1-pass FSPed composite, and (c) 3-pass FSPed composite surface after corrosion test

identified as CuCl, ZnO, and Cu_2O in the patterns of the corroded surface. Despite their low intensity, they indicate that the thickness of the corroded layer after the corrosion test is too thin to determine all components formed in the corrosion test.

4. Conclusion

This study addressed the microstructure and corrosion performance of the Cu-40wt%Zn alloy and its surface composite reinforced with Ti_2SC MAX phase. The main results could be summarized as follows:

(1) Applying 1-pass FSP on 60-40 brass alloy resulted in grain refinement. A further increase in the pass number to 3 led to more grain growth. The Ti_2SC MAX phase particles inhibited grain growth; after 3 passes of the FSP, the stir zone had fine and equiaxed grains. The homogeneous distribution of Ti_2SC particles in the brass matrix can be easily achieved by FSP.
(2) Based on the polarization test findings, all FSPed specimens showed higher corrosion current density. It means that the corrosion rate of the FSPed samples was continuously increased, and the corrosion rate of base metal was the minimum. The corrosion current density of brass alloy was 12.5 $\mu A.cm^{-2}$, while this value exceeded 30 $\mu A.cm^{-2}$ after FSP in all FSPed specimens.
(3) The cyclic polarization clearly showed that the pitting corrosion resistance of FSPed specimens is also more than that of the base metal. Moreover, the susceptibility of the FSPed samples to pitting corrosion was increased by the number of FSP passes. The pitting corrosion resistance of the FSPed samples decreased with an increment in the number of passes.
(4) The EIS measurements showed the lower electrochemical corrosion resistance of the FSPed samples compared to the base material, indicating lower corrosion protection for FSPed samples. With increasing number of passes, the corrosion resistance of the FSPed samples decreased. Also, the incorporation of Ti_2SC particles in the structure caused a decline in corrosion resistance of all FSPed samples.
(5) The capacitances range was calculated by three models, and this value enhanced in the order of power law (P-L) model> Brug's model> H-M model. Also, the values of film layer thickness were measured using C_{dl} values based on the proposed models. The Brug's model is the only approach that predicts the thickness of the film layer on the brass alloys similar to the reported values in the literature.

Reference

1. H. Yan, M.R.B. Abdul Rashid, S.Y. Khew, F. Li and M. Hong, Wettability Transition of Laser Textured Brass Surfaces inside Different Mediums, *Appl. Surf. Sci.*, 2018, **427**, p 369–375.
2. H. Jie, Q. Xu, L. Wei and Y.L. Min, Etching and Heating Treatment Combined Approach for Superhydrophobic Surface on Brass Substrates and the Consequent Corrosion Resistance, *Corros. Sci.*, 2016, **102**, p 251–258.
3. W.H. De Jong, E. De Rijk, A. Bonetto, W. Wohlleben, V. Stone, A. Brunelli, E. Badetti, A. Marcomini, I. Gosens and F.R. Cassee, Toxicity of Copper Oxide and Basic Copper Carbonate Nanoparticles after Short-Term Oral Exposure in Rats, *Nanotoxicology*, 2019, **13**(1), p 50–72.
4. F. Gapsari, Andoko and H. Wijaya, Corrosion Behavior of Brass in Nitric Acid, *Metal. Silicon*, 2018, **57**(4), p 333–336.
5. R. Davalos-Monteiro, Observations of Corrosion Product Formation and Stress Corrosion Cracking on Brass Samples Exposed to Ammonia Environments, *Mater. Res.*, 2019, **22**(1), p 1–10.
6. C.Y. Hung, C.M. Lin, C.C. Hsieh, C.C. Li, P.T.Y. Wu, K.T. Chen and W. Wu, A Novel Approach to Improving Resistance to Dezincification of Diphasic Brass, *J. Alloys Compd.*, 2016, **671**, p 502–508.
7. E.A.A. El Meguid and N.K. Awad, Electrochemical Pitting Corrosion Behaviour of a -Brass in LiBr Containing Solutions, *Corros. Sci.*, 2009, **51**(5), p 1134–1139.
8. J. Dominic, G. Perumal, H.S. Grewal and H.S. Arora, Facile Fabrication of Superhydrophobic Brass Surface for Excellent Corrosion Resistance, *Surf. Eng.*, 2020, **36**(6), p 660–664.
9. Z. Yu, C. Zhou, R. Liu, Q. Zhang, J. Gong, D. Tao and Z. Ji, Fabrication of Superhydrophobic Surface with Enhanced Corrosion Resistance on H62 Brass Substrate, *Coll. Surf. A Physicochem. Eng. Asp.*, 2020, **589**, p 124475.
10. H.Q. Fan, D.D. Shi, M.M. Ding, M.C. Li, Y.F. Cheng and Q. Li, Preparation of (3-Mercaptopropyl)Trimethoxylsilane Film on Brass and Its Corrosion Resistance in Natural Seawater, *Prog. Org. Coatings*, 2020, **138**, p 105392.
11. A. Robin, G.A.S. Martinez and P.A. Suzuki, Effect of Cold-Working Process on Corrosion Behavior of Copper, *Mater. Des.*, 2012, **34**, p 319–324.
12. M.A. Almomani, W.R. Tayfour and M.H. Nimrat, Effect of Silicon Carbide Addition on the Corrosion Behavior of Powder Metallurgy Cu-30Zn Brass in a 3.5 Wt.% NaCl Solution Mohammed, *J. Alloys Compd.*, 2016 https://doi.org/10.1016/j.jallcom.2016.04.006
13. A. Chraka, I. Raissouni, N. Benseddik, S. Khayar, A. Ibn Mansour, H. Belcadi, F. Chaouket and D. Bouchta, Aging Time Effect of *Ammi Visnaga* (L.) Lam Essential Oil on the Chemical Composition and Corrosion Inhibition of Brass in 3% NaCl Medium. Experimental and Theoretical Studies, *Mater. Today Proc.*, 2020, **22**, p 83–88.
14. M. Damej, D. Chebabe, S. Abbout, H. Erramli, A. Oubair and N. Hajjaji, Corrosion Inhibition of Brass 60Cu–40Zn in 3% NaCl Solution by 3-Amino-1, 2, 4-Triazole-5-Thiol, *J. Heliyon*, 2020 https://doi.org/10.1016/j.heliyon.2020.e04026
15. D. Chebabe, M. Damej, A. Dermaj, A. Oubair, H. Benassaoui, H. Erramli, N. Hajjaji and A. Srhiri, Corrosion Inhibition of Brass in 3% NaCl Solution by Electrosynthesized Poly 4- Amino-3-Méthyl-1,2,4-Triazole-5-Thione D, *Anal. Bioanal. Chem. Res.*, 2020, **7**(3), p 389–401.

16. L.A. Dobrzański and K. Lukaszkowicz, Comparison of Structure and Properties of the PVD Hybrid (Galvanic + PVD) and Galvanic Coatings Deposited onto the Brass Substrate, *Mater. Sci. Forum*, 2008, **591**, p 860–864.
17. M. Es-Saheb, E.S.M. Sherif, A. El-zatahry, M.M.E. Rayes and K.A. Khalil, Corrosion Passivation in Aerated 3.5% NaCl Solutions of Brass by Nanofiber Coatings of Polyvinyl Chloride and Polystyrene, *Int. J. Electrochem. Sci.*, 2012, **7**(11), p 10442–10455.
18. S. Das, S. Jena, S. Banthia, A. Mitra, S. Das and K. Das, Novel Pulse Potentiostatic Electrodeposition Route for Obtaining Pure Intermetallic Cu5Zn8-CuZn Composite Coating Using Glycerol-NaOH Based Electrolyte with Advanced Scratch Resistance and Anti-Corrosive Properties, *J. Alloys Compd.*, 2019, **792**, p 770–779.
19. Z.Y. Ma, Friction Stir Processing Technology: A Review, *Metall. Mater. Trans. A*, 2008, **39**(3), p 642–658. https://doi.org/10.1007/s11661-007-9459-0
20. K. Meena, A. Kumar and S.N. Pandya, Optimization of Friction Stir Processing Parameters for 60/40 Brass Using Taguchi Method, *Mater. Today Proc.*, 2017, **4**(2), p 1978–1987.
21. P.B. Joshi, R.H. Patel, P.S. Krishnan, V.L. Gadgeel, V.K. Kaushik and P. Ramakrishnan, Powder Metallurgical Silver-Metal Oxide Electrical Contacts by an Electroless Coating Process, *Adv. Powder Technol.*, 1996, **7**(2), p 121–130.
22. T.S. Mahmoud, Effect of Friction Stir Processing on Electrical Conductivity and Corrosion Resistance of AA6063-T6 Al Alloy, *Proc. Inst. Mech. Eng. Part C J. Mech. Eng. Sci.*, 2008, **222**(7), p 1117–1123.
23. M.W. Barsoum, *MAX Phases: Properties of Machinable Ternary Carbides and Nitrides*, Wiley-VCH, Weinheim, 2013
24. C. Guan and N. Sun, Synthesis and Tribological Properties of High Purity Ti2SC Nanolamellas by Microwave Hybrid Heating, *J. Alloys Compd.*, 2017, **699**, p 25–30. https://doi.org/10.1016/j.jallcom.2016.12.329
25. S.M. Hoseini, A. Heidarpour and S. Ghasemi, On the Mechanism of Mechanochemical Synthesis of Ti2SC from Ti/FeS2/C Mixture, *Adv. Powder Technol.*, 2019, **30**, p 1672–1677.
26. S.M. Hosseini, A. Heidarpour and S. Ghasemi, Effects of Ball Milling Sequences on the In-Situ Reactive Synthesis of the Ti2SC MAX Phase, *Adv. Appl. Ceram.*, 2020 https://doi.org/10.1080/17436753.2020.1732637
27. A. Heidarzadeh, B. Taghizadeh and A. Mohammadzadeh, Microstructure and Mechanical Properties of CuZn-Al2O3 Nanocomposites Produced by Friction Stir Processing, *Arch. Civ. Mech. Eng.*, 2020, **20**(3), p 1–12. https://doi.org/10.1007/s43452-020-00102-5
28. M.M. Jalilvand, Y. Mazaheri, A. Heidarpour and M. Roknian, Development of A356/Al 2 O 3 + SiO 2 Surface Hybrid Nanocomposite by Friction Stir Processing, *Surf. Coatings Technol.*, 2019, **360**, p 121–132.
29. A. Heidarzadeh, A. Chabok, V. Klemm and Y. Pei, A Novel Approach to Structure Modification of Brasses by Combination of Non-Equilibrium Heat Treatment and Friction Stir Processing, *Metall. Mater. Trans. A Phys. Metall. Mater. Sci.*, 2019, **50**(5), p 2391–2398. https://doi.org/10.1007/s11661-019-05175-3
30. S. Karimi, A. Ghahreman and F. Rashchi, Kinetics of Fe(III)-Fe(II) Redox Half-Reactions on Sphalerite Surface, *Electrochim. Acta*, 2018, **281**, p 624–637.
31. C. Op’t Hoog, N. Birbilis and Y. Estrin, Corrosion of Pure Mg as a Function of Grain Size and Processing Route, *Adv. Eng. Mater.*, 2008, **10**(6), p 579–582.
32. R.S. Mishra, Z.Y. Ma and I. Charit, Friction Stir Processing: A Novel Technique for Fabrication of Surface Composite, *Mater. Sci. Eng. A*, 2003, **341**, p 307–310.
33. Y. Mazaheri, A. Heidarpour, M.M. Jalilvand and M. Roknian, Effect of Friction Stir Processing on the Microhardness, Wear and Corrosion Behavior of Al6061 and Al6061/SiO2 Nanocomposites, *J. Mater. Eng. Perform.*, 2019, **28**(8), p 4826–4837.
34. M. Rahsepar and H. Jarahimoghadam, The Influence of Multipass Friction Stir Processing on the Corrosion Behavior and Mechanical Properties of Zircon-Reinforced Al Metal Matrix Composites, *Mater. Sci Eng. A*, 2016, **671**, p 214–220.
35. L. Lv, X. Jiang, X. Xiao, H. Sun, Z. Shao and Z. Luo, Study on Corrosion Resistance of Copper Matrix Composites Reinforced by Al2O3 Whiskers, *Mater. Res. Express*, 2020, **7**(2), p 26534.
36. Q.N. Song, N. Xu, X. Jiang, Y. Liu, Y. Tong, J.S. Li, Y.F. Bao and Y.X. Qiao, Effect of Sulfide Concentration on the Corrosion and Cavitation Erosion Behavior of a Manganese-Aluminum Bronze in 3.5% NaCl Solution, *J. Mater. Eng. Perform.*, 2019, **28**(7), p 4053–4064.
37. T. Kosec, I. Milošev and B. Pihlar, Benzotriazole as an Inhibitor of Brass Corrosion in Chloride Solution, *Appl. Surf. Sci.*, 2007, **253**(22), p 8863–8873.
38. Y. Li, J.B. He, M. Zhang and X.L. He, Corrosion Inhibition Effect of Sodium Phytate on Brass in NaOH Media. Potential-Resolved Formation of Soluble Corrosion Products, *Corros. Sci.*, 2013, **74**, p 116–122.
39. S.S.A. El-Rehim, F.H. Assaf, A. El Sayed, M.M.A. Krisha and A.M. Zaky, Anodic and Cathodic Behaviour of α-Brass in Na2SO4 Solutions, *Mater. Trans. JIM*, 1995, **36**(6), p 770–773.
40. T.K. Mikić, I. Milošev and B. Pihlar, Passivity and Corrosion of Cu-XZn (x 10–40 Wt%) Alloys in Borate Buffer Containing Chloride Ions, *J. Appl. Electrochem.*, 2005, **35**(10), p 975–984.
41. R. Ravichandran and N. Rajendran, Influence of Benzotriazole Derivatives on the Dezincification of 65–35 Brass in Sodium Chloride, *Appl. Surf. Sci.*, 2005, **239**(2), p 182–192.
42. A.G. Gad-Allah, M.M. Abou-Romia, M.W. Badawy and H.H. Rehan, Passivity of α-Brass (Cu:Zn/67:33) and Its Breakdown in Neutral and Alkaline Solutions Containing Halide Ions, *J. Appl. Electrochem.*, 1991, **21**(9), p 829–836.
43. M.R.G. de Chialvo, R.C. Salvarezza, D. Vasquez Moll and A.J. Arvia, Kinetics of Passivation and Pitting Corrosion of Polycrystalline Copper in Borate Buffer Solutions Containing Sodium Chloride, *Electrochim. Acta*, 1985, **30**(11), p 1501–1511.
44. S.M. AbdelHaleem, Effect of Alkali Concentration Figure 1 Shows Typical CVs of the Copper Electrode in 1 M NaOH Traced at A, *Solutions*, 1981, **117**, p 309–319.
45. J. Morales, G.T. Fernandez, S. Gonzalez, P. Esparza, R.C. Salvarezza and A.J. Arvia, A Comparative Study of the Passivation and Localized Corrosion of α-Brass and β-Brass in Borate Buffer Solutions Containing Sodium Chloride: III. The Effect of Temperature, *Corros. Sci.*, 1998, **40**(2–3), p 177–190.
46. M. Kabasakaloğlu, T. Kiyak, O. Şendil and A. Asan, Electrochemical Behavior of Brass in 0.1 M NaCl, *Appl. Surf. Sci.*, 2002, **193**(1–4), p 167–174.
47. H.H. Strehblow and B. Titze, The Investigation of the Passive Behaviour of Copper in Weakly Acid and Alkaline Solutions and the Examination of the Passive Film by Esca and Iss, *Electrochim. Acta*, 1979, **25**, p 839–850.
48. C.B. Smith, M.W. Mahoney, G.R. Argade and R.S. Mishra, Effect of Friction Stir Processing on Corrosion Behavior of AA5083 Aluminum Alloy, *Friction Stir Welding and Proceesing VI*. R. Mishra, M.W. Mahoney, Y. Sato, Y. Hovanski, R. Verma Ed., Wiley, 2011, p 307–313
49. I. Milošev and M. Metikoš-Huković, Effect of Chloride Concentration Range on the Corrosion Resistance of Cu-XNi Alloys, *J. Appl. Electrochem.*, 1999, **29**(3), p 393–402.
50. I. Milošev, Breakdown of Passive Film on Copper in Bicarbonate Solutions Containing Sulfate Ions, *J. Electrochem. Soc.*, 1992, **139**(9), p 2409.
51. S. Esmailzadeh, M. Aliofkhazraei and H. Sarlak, Interpretation of Cyclic Potentiodynamic Polarization Test Results for Study of Corrosion Behavior of Metals: A Review, *Prot. Met. Phys. Chem. Surf.*, 2018, **54**(5), p 976–989.
52. M.M. Sadawy and M. Ghanem, Grain Refinement of Bronze Alloy by Equal-Channel Angular Pressing (ECAP) and its Effect on Corrosion Behaviour, *Def. Technol.*, 2016, **12**(4), p 316–323.
53. S. Karimi, A. Ghahreman, F. Rashchi and J. Moghaddam, The Mechanism of Electrochemical Dissolution of Sphalerite in Sulfuric Acid Media, *Electrochim. Acta*, 2017, **253**, p 47–58. https://doi.org/10.1016/j.electacta.2017.09.040
54. Y.-K. Wei, X.-T. Luo, Y. Ge, X. Chu, G.-S. Huang and C.-J. Li, Deposition of Fully Dense Al-Based Coatings via in-Situ Micro-Forging Assisted Cold Spray for Excellent Corrosion Protection of AZ31B Magnesium Alloy, *J. Alloys Compd.*, 2019, **806**, p 1116–1126.
55. J. Liu, K. Zhao, M. Yu and S. Li, Effect of Surface Abrasion on Pitting Corrosion of Al-Li Alloy, *Corros. Sci.*, 2018 https://doi.org/10.1016/j.corsci.2018.04.010
56. K. Surekha, B.S. Murty and K. Prasad Rao, Comparison of Corrosion Behaviour of Friction Stir Processed and Laser Melted AA 2219 Aluminium Alloy, *Mater. Des.*, 2011, **32**(8–9), p 4502–4508. https://doi.org/10.1016/j.matdes.2011.03.033

57. I. Miloševa and T. Koseca, Electrochemical and Spectroscopic Study of Benzotriazole Films Formed on Copper, Copper-Zinc Alloys and Zinc Inchloride Solution, *Chem. Biochem. Eng. Q.*, 2009, **23**(1), p 53–60.
58. M. Mohammadi, L. Choudhary, I.M. Gadala and A. Alfantazi, Electrochemical and Passive Layer Characterizations of 304L, 316L, and Duplex 2205 Stainless Steels in Thiosulfate Gold Leaching Solutions, *J. Electrochem. Soc.*, 2016, **163**(14), p C883–C894. https://doi.org/10.1149/2.0841614jes
59. L.P. Kazansky, Y.E. Pronin and I.A. Arkhipushkin, XPS Study of Adsorption of 2-Mercaptobenzothiazole on a Brass Surface, *Corros. Sci.*, 2014, **89**, p 21–29. https://doi.org/10.1016/j.corsci.2014.07.055
60. I. Milošev, T.K. Mikić and M. Gaberšček, The Effect of Cu-Rich Sub-Layer on the Increased Corrosion Resistance of Cu–XZn Alloys in Chloride Containing Borate Buffer, *Electrochim. Acta*, 2006, **52**(2), p 415–426. https://doi.org/10.1016/j.electacta.2006.05.024